



Compaction and sintering effects on scaling law of permeability-porosity relation of powder materials

Zhiguo Tian^a, Duzhou Zhang^{b,*}, Gang Zhou^b, Shaohua Zhang^b, Moran Wang^{a,*}

^a Department of Engineering Mechanics, Tsinghua University, Beijing 100084, China

^b Beijing Institute of Control Engineering, Beijing, China

ARTICLE INFO

Keywords:

Cold compaction
Solid-state sintering
Pore-scale modeling
Permeability

ABSTRACT

Analysis and understanding of the permeability-porosity relationship of powder materials by cold compaction and solid-state hot sintering is very important for material design and optimization. This work presents a pore-scale numerical framework, including a discrete element method for powder cold compaction, a cellular automata algorithm with curvature-driving redistribution for solid-state hot sintering and a lattice Boltzmann method for fluid flow simulation, to study the permeability-porosity relationship of materials by cold compaction and solid-state hot sintering processes. The results show that the cubic scaling law always holds for the porous materials by cold compaction, while the hot sintering process decreases the permeability dramatically at low porosity. An exponential decay function has been proposed as a correction factor to the permeability-porosity relationship of materials by compaction & sintering processes, which predicts the permeability asymptotically approaching to the cubic scaling law at high porosity while agreeing well with both numerical and experimental data at low porosity. The microstructure evolution analysis shows that the small pores that connect large pores may vanish by sintering, which causes the remarkable permeability decrease at low porosity. The excellent agreements between the numerical predictions and the experimental measurements suggest that the proposed numerical framework provides a powerful tool for analysis and optimization of material designs.

1. Introduction

Cold compaction and solid-state hot sintering of powders, which can produce microporous media, are common processes that coexist in nature and modern industry, such as the plastic flow of rock matrix in crust and volcano [1–4], the powder metallurgy at a mild temperature using metals and polymers [5–8], and so on. The solid-state hot sintering means the temperature is below the melting point of the powder material. The permeability of the produced microporous media receives increasing attentions in recent years [9–17]. Among them, the relationship between the permeability and porosity has been pursued for a long time, since they are two key macroscopic physical parameters and can easily relate to many other mechanical parameters for engineering applications [14,16,18]. Intuitively, physical processes, like the plastic deformation of single powder in cold compaction and the molecular diffusion among powders in solid-state hot sintering, are responsible for the change of porosity, permeability and subsequently their relationship. It has been found that the permeability is proportional to the power of porosity [19,20], named as the scaling law of the

permeability-porosity relationship in this work, and the value of the power is generally three [1,19,21–25]. However, when the porosity is below a certain value [1,26], the permeability has been proved experimentally to decrease dramatically, even several orders of magnitude, while the porosity only reduces a little bit. This phenomenon may be critical in timescale relevant to magma rise and eruption [27]. Some attempts want to fit a universal scaling law by data collection and rearrangement, only changing the value of the power [14], but the fitting result has large fluctuations compared with the actual experimental data and cannot truly capture the nature of sudden change at very low porosity. The underlying mechanism and general structural details to account for the breakdown of the scaling cubic law are still lacking and need to be revealed.

Experimental studies, including direct imaging using the X-ray computed tomography [9,28,29], scanning electron microscopy [11–14, 30,31] and transmission electron microscopy [32], are conducted to get the internal pore structures. Then the structures are used for explaining the experimental permeability results qualitatively or as input for numerical permeability simulation. But such methods are obviously

* Corresponding authors.

E-mail address: mrwang@tsinghua.edu.cn (M. Wang).

<https://doi.org/10.1016/j.ijmecsci.2023.108511>

Received 21 December 2022; Received in revised form 27 May 2023; Accepted 30 May 2023

Available online 30 May 2023

0020-7403/© 2023 Elsevier Ltd. All rights reserved.

expensive and more importantly, can only study case by case, lacking power to reveal the underlying mechanism. Besides, the current most advanced technology of microscope is still very hard to fully obtain the three-dimensional structural details of tight samples, both at a clear enough resolution and a big enough view, to capture the dynamic deformation of micropore shapes experimentally. Others turn to phenomenological approach [14,27,33], which can provide fitting formulas for macroscopic parameters, like density and permeability, in relation to compressing pressure, sintering temperature and time, but this is shortage of microscopic structural details and the mechanisms of solid-state sintering proposed by material physicists [33–35], including the bulk diffusion and surface diffusion, cannot deal with very low porosity.

Numerical simulation is extensively used to carry out parametric discussions which is expected to be able to reveal the main mechanism. Interestingly, the physical processes and parameters that we are concerned with in this work belong to the intersection between the solid and fluid mechanics, in which mechanical responses and flow processes are concerned with separately. Finite element method is a powerful tool to investigate the cold compaction and solid-state sintering of powders [36, 37], but the representative element volume differs quite enormously for mechanical responses and permeability variation [38]. Generally, the representative element volume is much larger for studying permeability variation, which is beyond the capabilities of the finite element method.

The pore network model is an alternative with capacity to study larger packings and has been adopted to partially recover this phenomenon, while this method needs predefined pore size distribution which is got by experimental measurement and is a posteriori [21,37]. Discrete element method [39–46] and phase-field method [42,47] are good potentials for recovering the microscopic structural evolution without structure input and dealing with enough powders. But affordable algorithm and code implementation need great effort. As for the fluid flow simulation to get the permeability, the lattice Boltzmann method is powerful in studying the fluid flow in microporous media [48]. Unfortunately, since this problem lies in the cross field, none effort of combining these potential methods together has been taken to tackle it. A feasible numerical simulation framework, which can capture the main structural characteristic in the cold compaction and solid-state hot sintering processes of powders and accurately realize the fluid flow simulation, should be proposed if we attempt to cope with this problem.

To fill these gaps in knowledge, in this work, a pore-scale numerical modeling method, including the discrete element method (DEM), a cellular automata algorithm and a lattice Boltzmann method (LBM), for studying the cold compaction and solid-state hot sintering, is developed in Section 2. The geometry change of pores will be naturally captured and the global pore size distribution will be analyzed to provide direct evidence for the breakdown of scaling law, in Section 3, and thus a full correlation will be presented. The conclusion will be drawn in Section 4.

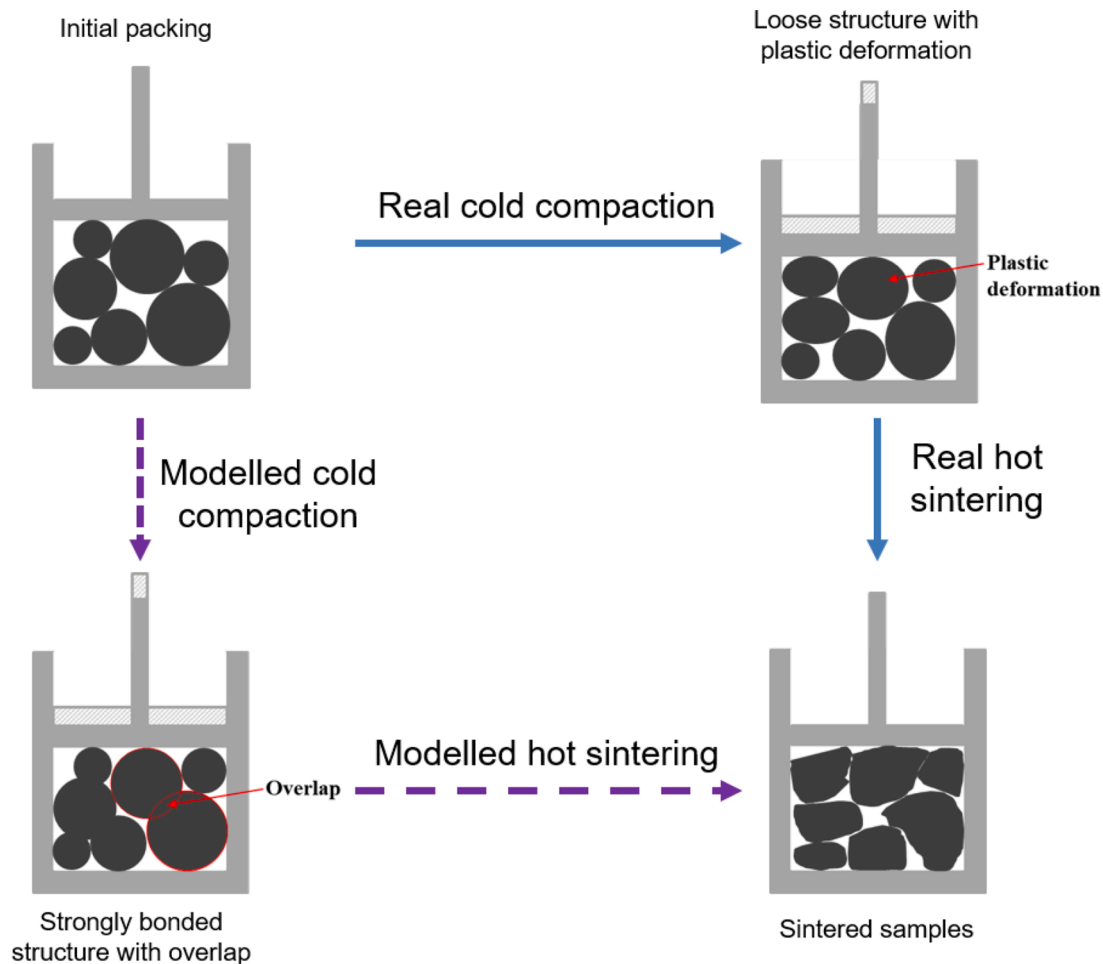


Fig. 1. The schematic of simulation strategy for the hot sintering process. The solid arrows show the real fabrication process. The powders are put in a cubic holder. In the loose structure, the piston is pushed downward to compact the spherical powders with plastic deformation. The compacted structure is then sintered and the powders release to irregular shape due to high temperature in the sintering process. This real fabrication process is modeled in the simulation process as the dashed arrows shows. In the strongly bonded structure, the spherical powders can overlap with each other to approximate the compaction process. In the hot sintering process, the overlapping area is redistributed according to the principle of preferentially filling the position with the smallest spatial curvature in the pore area and the principle of mass conservation, to recover irregular shape caused by the sintering process.

2. Numerical methods

In this section, the basic strategy of our pore-scale simulation framework is introduced. The main ideas and the simulation flowchart, including the discrete element method, the cellular automata algorithm and the lattice Boltzmann method, are presented subsequently.

2.1. Basic strategy and idea

The simulation strategy for modeling the cold compaction and solid-state hot sintering processes is shown in Fig. 1. In the actual sintering process, the powders are not perfect spheres and they are plastically deformed in the cold compaction process. Besides, in the solid-state sintering, there is plastic flow due to the molecular diffusion caused by high temperature. These actual physical processes cannot be numerically simulated unless enormous computational sources are used. We adopt a three-step assumption and rule in this work. For the first step, the powder is assumed to be spherical. Second step, the spheres can overlap without any deformation, to simulate the compaction process based on the discrete element method. At the third step, the overlapping volume is redistributed according to the principle of preferentially filling the position with the smallest spatial curvature in the pore area, to simulate the solid-state sintering process. The implementation process is described in detail as follows.

2.2. Discrete element method (DEM)

The discrete element method is a first-principles method for granular materials that treats each particle individually. It originates from the great demand for simulating the industrial processes including powders: 50% of industrial products and 75% of raw materials are powders [49]. After the pioneering work of Cundall et al. [40,44] in the 1980s, DEM was developed rapidly, because the explicit time integration scheme was introduced, which is constrained by the limitation of the time step. This greatly improved the efficiency, which directly gave new birth to this method and promoted the wide applications [50–52].

The implementation process of DEM is illustrated by taking spherical particles as an example, including:

- i Calculate the overlap distance between individual particles. This is simply realized by comparing the distance of two sphere centers with the sum of two radii.
- ii Calculate the contact force between individual particles. When there is contact between particles and the overlap distance is greater than zero, the contact force between particles needs to be calculated. The contact force models are divided into two categories: one is the linear spring damping model proposed by Cundall et al. [40,44]. In this type, the magnitude of the normal contact force is proportional to the overlap distance δ ; the other is the Hertz-Mindlin model [53,54] and its variations, in which the normal contact force is proportional to the 1.5 power of the overlap distance $\delta^{1.5}$. Basic Hertz-Mindlin model assumes the contact surface is elliptical and derives the subsequent expression for the relationship between contact force and overlap length analytically. It is more physical than the Cundall model. The contact force model is summarized in detail in Ref. [55] and is the core step of the entire process. For different materials, different contact force models need to be used, and the parameters in the models need to be tediously calibrated.
- iii Calculate the resultant force on each particle. In addition to the contact force, particles may be subjected to other forces, such as gravity, van der Waals forces, drag forces in gas-solid or liquid-solid two-phase flows, electric field forces between charged particles and so on. A summary of these forces can be found in Ref. [56].
- iv Update the position of each particle according to the Newton's second law. The motion of each particle is a uniformly accelerated linear motion in each time step.

v Advance to the next time step.

Those are the basic idea and the calculation process of DEM. In this work, we adopt it to simulate the cold compaction process of spherical packing. For general particle shapes, spheropolyhedra method [57,58] can be sought to.

2.3. Cellular automata with curvature-driving redistribution

In the hot solid-state sintering process, the temperature field is usually formed by a bulk heating except for the laser heating. Therefore, both the structure of powder packing and the temperature rise can be assumed to be homogeneous so that the thermodynamic properties are homogeneous. In the small pores and the near region to the contacts, the surface tension is the main driving force for structure redistribution of the overlapping parts. As well known, the surface tension depends on the curvature of each spot which is still very hard to obtain for a real geometry. Here for a digitalized system represented by binarized points, 0 for void and 1 for solid, the curvature of each point is simplified to be proportional to the point number, as shown in Fig. 2(a). The red frame is the nearby points of the red circle dot and the blue frame is the nearby points of the blue rectangular dot. The curvature is then calculated by counting the pore lattice number [59]. The principle of preferentially filling the position with the smallest spatial curvature in the pore area is put forward in this work. That means that, illustrated by the two-dimensional diagram in Fig. 2(a), the red dot is occupied with priority by the volume/point in the overlapping area. Following this rule, the neck grows between two contacting spheres as shown in Fig. 2 (b), which appears consistent with the classic theory [33,34]. The 2D slices in time sequence of 3D simulation are shown in Fig. 3 and the neck formation matches well with the classical sintering theory.

2.4. Lattice Boltzmann method (LBM)

The lattice Boltzmann method is a numerical method for simulating fluid flow processes based on evolution of particle distributions. LBM is based on the lattice Boltzmann equation, which can regress to the Navier-Stokes equation via Chapman-Enskog multiscale expansion, and thus makes the fluid flow numerically solved [60]. The implementation process of LBM is illustrated below.

The lattice Boltzmann equation can be written as:

$$f_i(\mathbf{x} + \mathbf{c}_i \Delta t, t + \Delta t) = f_i(\mathbf{x}, t) + \Omega_i(\mathbf{x}, t), \quad (1)$$

where $f_i(\mathbf{x}, t)$ is the density distribution function which means the particle density in the position \mathbf{x} and the time t ; \mathbf{c}_i is the discrete velocity and i is the direction of the discrete velocity; $\Omega_i(\mathbf{x}, t)$ is the collision term; Δt is the time interval. The discrete density distribution function satisfies that:

$$\sum_i f_i(\mathbf{x}, t) = \rho(\mathbf{x}, t), \quad \sum_i \mathbf{c}_i f_i(\mathbf{x}, t) = \rho \cdot \mathbf{u}(\mathbf{x}, t), \quad (2)$$

where ρ is the fluid density and \mathbf{u} is the fluid velocity.

The most popular form of the collision term is the Bhatnagar-Gross-Krook (BGK) approximation, which is expressed as:

$$\Omega_i(f) = \frac{f_i - f_i^{eq}}{\tau} \Delta t, \quad (3)$$

where τ is the relaxation time which is related to the kinetic viscosity of fluid [61]; f_i^{eq} is the equilibrium density distribution function, whose form is:

$$f_i^{eq} = \omega_i \rho \left(1 + \frac{3\mathbf{u} \cdot \mathbf{c}_i}{c^2} + \frac{(9\mathbf{u} \cdot \mathbf{c}_i)^2}{2c^4} - \frac{3\mathbf{u} \cdot \mathbf{u}}{2c^2} \right), \quad (4)$$

where ω_i is the weight function; c is the lattice speed.

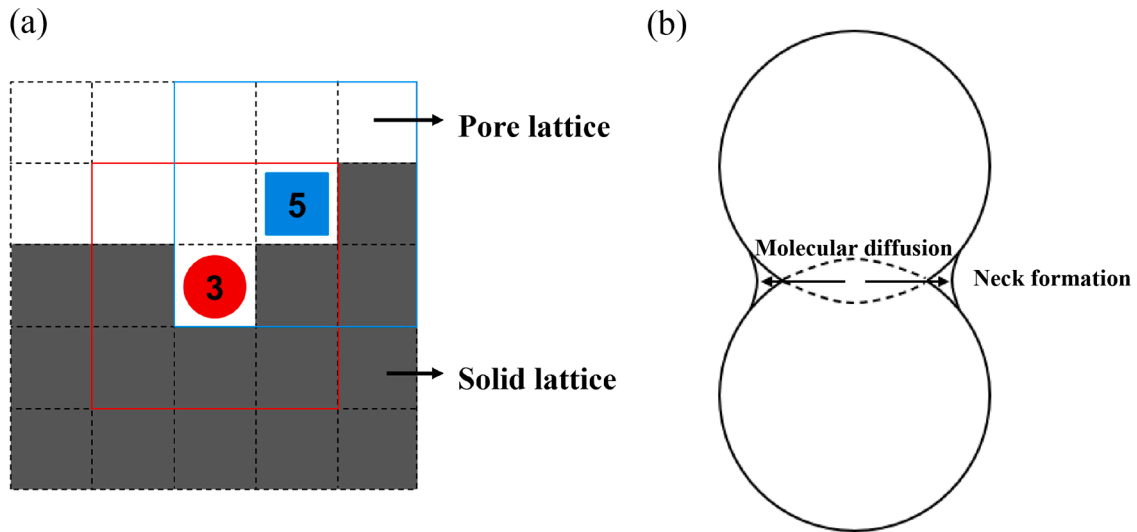


Fig. 2. Diagram of algorithm for the curvature-driving sintering. (a) shows the lattice number for calculating the curvature. The dark area and the white area represent the solid lattice and the pore lattice respectively. The red solid circle and the nearby red box with solid line is a pore lattice and its calculation area of curvature. The number “3” means there are 3 pore lattices near this red solid circle. The blue solid box and the nearby blue box with solid line is another pore lattice and its calculation area of curvature. The number “5” means there are 5 pore lattices near this blue solid box. Therefore, in the whole area of (a), the smallest curvature is the red solid circle and it is preferentially filled by the overlapping area between powders in the simulation. (b) shows the diagram of two sintering spheres. The area with dashed line is the overlap area between the two spheres caused by the compaction process. The mass in the overlapping area is redistributed caused by molecular diffusion to form a neck area according to the calculation process of (a). The solid arrows show the mass redistribution process for the overlapping area to the neck area.

Combining Eq. (1) and formula (3) leads to:

$$f_i(\mathbf{x} + \mathbf{c}_i \Delta t, t + \Delta t) = f_i(\mathbf{x}, t) - \frac{\Delta t}{\tau} (f_i(\mathbf{x}, t) - f_i^{eq}(\mathbf{x}, t)). \quad (5)$$

The calculation of Eq. (5) is divided into two steps: a collision step and a streaming one. The collision step is:

$$f_i^*(\mathbf{x}, t) = f_i(\mathbf{x}, t) - \frac{\Delta t}{\tau} (f_i(\mathbf{x}, t) - f_i^{eq}(\mathbf{x}, t)), \quad (6)$$

and then the streaming step is:

$$f_i(\mathbf{x} + \mathbf{c}_i \Delta t, t + \Delta t) = f_i^*(\mathbf{x}, t). \quad (7)$$

The calculation steps of the lattice Boltzmann method are summarized as follows:

- i Calculate the fluid density ρ and the velocity \mathbf{u} based on Eq. (2);
- ii Calculate the equilibrium distribution function based on Eq. (4);
- iii Perform the collision step based on Eq. (6);
- iv Perform the streaming step based on Eq. (7);
- v Advance to the next time step.

More details of the derivation for the above process can be found in the classical papers and comprehensive reviews [62–66]. The two most distinctive features of LBM are: easy for parallel computing and suitable for calculation of flow in complex structures (especially porous media) [65–68] or in complicated processes [61,69–72], because the collision and streaming steps are performed independently among discrete points, and each discrete point stores more information [73,74].

The fundamentals and implementation process of the three numerical methods used in this paper have been introduced. The overall framework of the pore-scale numerical modeling proposed in this paper is shown in Fig. 3. The three dashed frames correspond to three processes, cold compaction, solid-state hot sintering and fluid flow, which are simulated by the three numerical methods above.

3. Results and discussion

In this section, the code verification is first presented. Subsequently, the parameters and the whole simulation process are described and given. An experimental study about the permeability measurement is introduced, to give experimental benchmark of our simulation results. The permeability-porosity relationship is established in a large porosity scope and the effects of cold compaction and solid-state hot sintering are investigated separately, which obey the same rule in large porosity and deviate dramatically in very small porosity. Convenient expressions for the permeability-porosity relationship are given. The structural details are obtained to account for the underlying pore-scale mechanism.

3.1. Code verifications

The numerical codes are verified by comparing with analytical solutions of either classic cases of sphere packing process or fluid flow through porous structures individually since there is no theoretical solution for coupling.

For the sphere packing process, the collision of two identical spheres is chosen to verify the contact force in DEM. In our paper, we consider the compaction process, in which the kinetic energy of spherical particle is omittable. Therefore, we choose the basic Hertz-Mindlin model, which doesn't consider the energy dissipation in the calculation. The explicit form of the Hertz-Mindlin model is:

$$F_n = \frac{2}{3} \frac{E}{1 - \nu_p^2} \left(\frac{R_0}{2} \right)^{0.5} d^{1.5} \quad (8)$$

The comparison between the analytical contact force values and the simulated values is well [75]. It is indicated that the DEM simulation can accurately capture the collision process, which verifies the correctness of the algorithm and code implementation of the Hertz-Mindlin contact force model.

For the fluid simulations through porous structures by LBM, the flow behavior through a faced-centered-cubic (FCC) structure [48] and a body-centered-cubic (BCC) structure [76] has been considered in our previous work. The results indicate that LBM can capture the flow

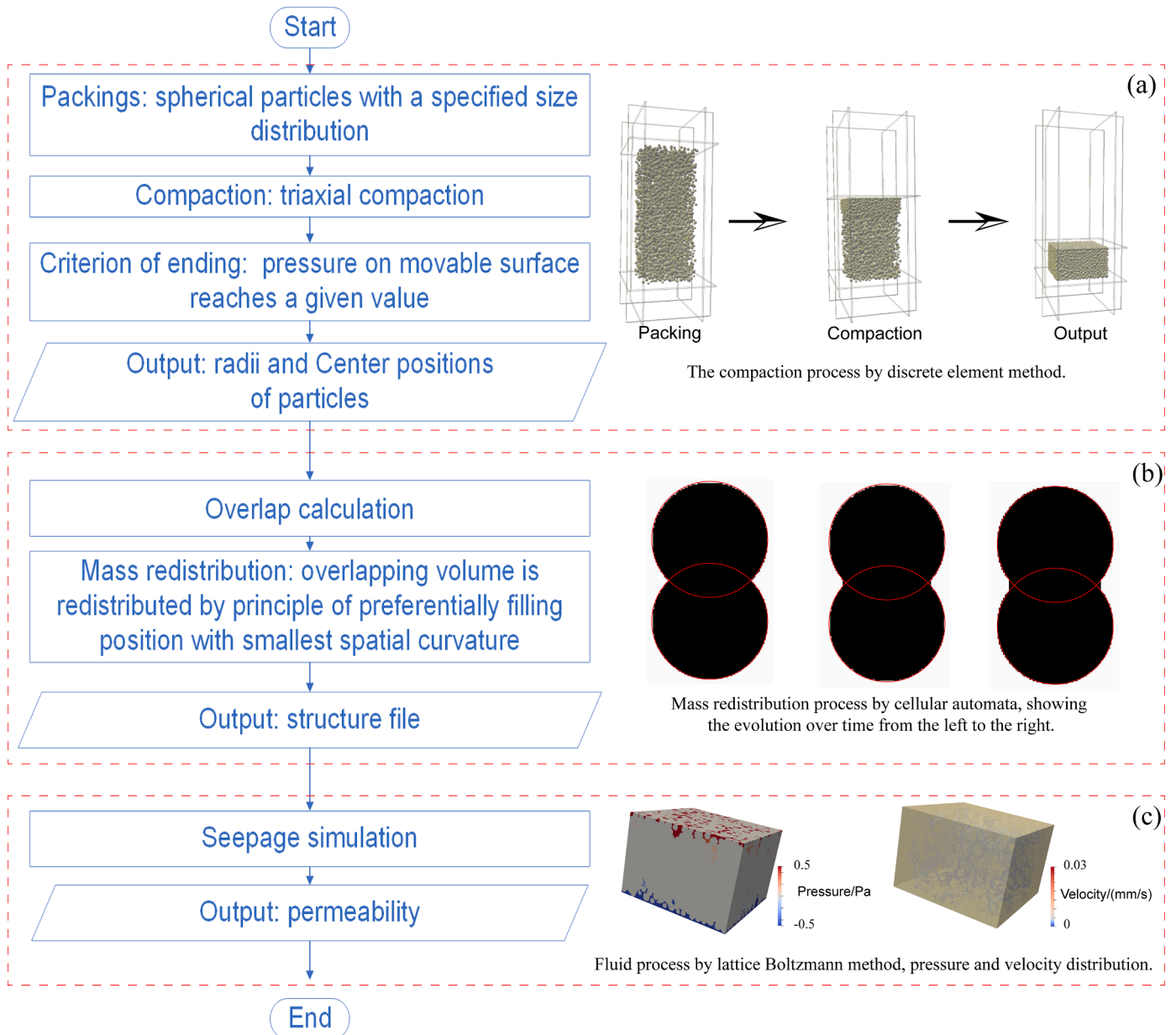


Fig. 3. Diagram of the pore-scale numerical modeling procedure, including (a) cold compaction, (b) solid-state hot sintering, and (c) fluid flow modeling processes. (a) The loose packing with a specified number and size distribution within the hexahedron area is generated and then compaction is conducted by triaxial compaction process. (b) The mass redistribution in hot sintering process by the cellular automata: the overlapping area between spherical particles caused by compaction is redistributed according to the principle of preferentially filling the position with the smallest spatial curvature in the pore area. The 2D slices in time sequence of 3D simulation, two overlapping spheres, are shown and the neck formation matches qualitatively with the classical sintering theory [34]. (c) The fluid flow simulation by LBM: on the porous structures with or without sintering, the transport governing equations will be numerically solved and the permeability is therefore determined.

behavior and calculate the permeability accurately as long as the resolution of geometry is fine enough. Further investigations also show that LBM requires much lower grid number for geometry resolution than the traditional CFD methods (the finite element method, the finite difference method etc.) at the same numerical accuracy [61,71,77].

3.2. Numerical simulations

After verification, the cold compaction and then solid-state hot sintering processes are numerically simulated.

First, the powder size distribution is appointed as a normal distribution, which may represent a common case in nature and industry. For the compaction process, implemented by DEM, the contact force model between particles is chosen as the Hertz-Mindlin Model, as Eq. (8)

shows. The compaction is accomplished by using the open-source code, Yade [75] and mimicking the three-axial compression in cuboid, which means fixing five facets of the cuboid and pressing the movable one to reach the assigned pressure value. The parameters used in DEM are

Table 1
The parameters used in the Discrete Element Method.

Properties	Values
Sphere diameter distribution	Normal distribution with a mean value at 25 μm
Frictional degree between spheres	25.00°
Young's modulus	2.50 GPa
Poisson's ratio	0.33
Density	1400.00 kg/m^3

shown in Table 1. After the cold compaction, different forms of packing are obtained with different porosity under different pressures. These structures of packing are used as inputs for the solid-state sintering process. This step will be skipped when only cold compaction is considered. No more parameters are introduced in this step, except that the overlapping volume caused by compaction needs to be captured for further redistributing. In this step, we write codes in MATLAB and have considered the intersection of more than two particles. For each particle, we output the contacting particles in its neighbouring region in DEM and use this information to calculate the overlap volume. As the last step, the flow process through the redistributed microstructure is simulated by a high-performance LBM and then the permeability will be calculated numerically [38]. In every simulation, 4000 particles whose mean radius is 25 μm are used in DEM and a box of 288 $\mu\text{m} \times 288 \mu\text{m} \times 210 \mu\text{m}$ is extracted, discarding the near-wall region, for LBM simulation. The spatial resolution of LBM code is 1 μm and subsequently, for each, 288 \times 288 \times 210 meshes are simulated. The imposed pressure difference is 1 Pa in the direction of 210 edge. The fluid material is water. The permeability of each packing for both cold compaction and solid-state hot sintering can be obtained nearly at the same time.

3.3. Experimental measurements

To figure out further mechanisms, experiments have been performed as well in this work. Porous materials are fabricated by cold compaction and solid-state hot sintering of polyimide powders in this work. The sintering process is implemented by a sintering furnace, in which the sintering temperature is fixed at 370 $^{\circ}\text{C}$. Different values of porosity, including 6.0%, 7.5%, 9.0% and 13.1%, are obtained by changing the compressive force and the sintering time. The compressive force is $1.5 \times 10^5 \text{ N}$, $1.3 \times 10^5 \text{ N}$, $1.1 \times 10^5 \text{ N}$ and $0.8 \times 10^5 \text{ N}$ and the sintering times are 2.5 h, 2.5 h, 2 h and 2 h correspondingly. The values of the porosity are measured by a Mercury Porometer, whose type is AutoPore IV 9510. The physical properties of the raw powders are the same as the values in Table 1.

The experimental set-up is shown in Fig. 4 and steady-state measurements are conducted to obtain the permeability. The samples are made into a cylindrical shape, whose diameter is 2.2 mm and length is 6.5 mm. Nitrogen is used as the test fluid. In the measurements, the downstream pressure remains at the atmospheric pressure and the upstream pressure is lifted and kept changeless. Under different pressure differences, the flow rate is measured by a flowmeter, whose minimum accuracy is 0.01 mL. In our experimental measurement, the permeability is smaller than 10^{-16} m^2 and the slippage effect needs to be considered. The slippage effect is characterized by the Knudsen number, Kn, whose definition is the ratio between the mean free path of the gas molecule and the characteristic pore size of the porous medium, and should be carefully considered for small Kn. Reflected in the experiments, the slippage effect makes the measured apparent permeability deviate from the prediction of the Darcy's law. Klinkenberg first studied the slippage effect of gas flow in porous media and demonstrated that for permeability smaller than 10^{-14} m^2 , the slippage effect should be eliminated by the Klinkenberg plot [68,78] as demonstrated by Fig. 5. For every

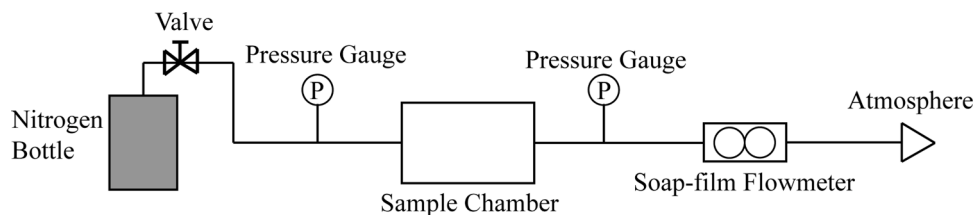


Fig. 4. Diagram of experimental set-up, including the Nitrogen bottle, valve, upstream pressure gage, sample chamber, downstream gage, soap-film flowmeter, and the downstream of the flowmeter being the atmosphere. The upstream pressure can be changed by the valve to a given value. The measured cylindrical sample is put in the sample chamber. Every sample is measured by several pressure differences and the Klinkenberg-plot is plotted to eliminate the slippage effect.

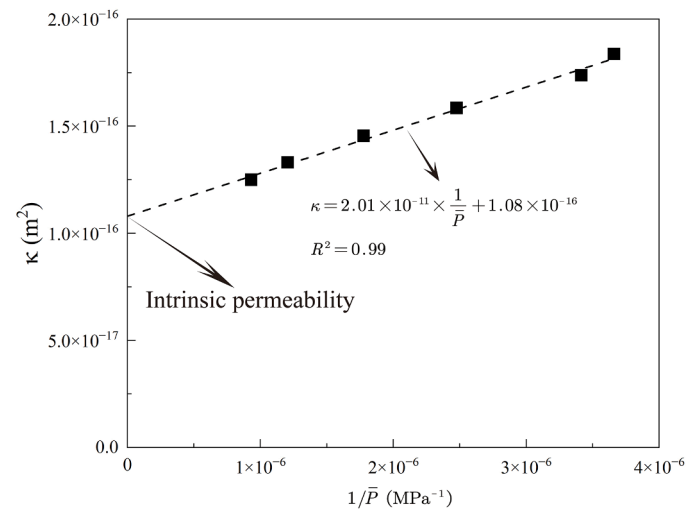


Fig. 5. Demonstration, using data of one sample with 13.1% porosity, of Klinkenberg plot for eliminating slippage effect. The horizontal axis is the reciprocal of the mean pressure and $\bar{P} = (P_u + P_d)/2$. The rectangular block is the experimental results and for each point, the permeability value is calculated by the integration form of the Darcy's law. The dash line is the fitting line, with a correlation coefficient $R^2=0.99$, whose intercept is the intrinsic permeability.

sample, different pressure gradients are imposed and the intrinsic permeability is calculated by the intercept in the plot of the apparent permeability versus the reciprocal of mean pressure. Here, the apparent permeability is calculated by the integration form of the Darcy's law: $\frac{P_u^2 - P_d^2}{2P_d L} = \frac{\mu}{\kappa_a} \frac{Q_d}{A}$, where P_u and P_d are the upstream and downstream pressure, Q_d is the volume flow rate in the downstream, A and L are the cross-sectional area and length of the sample, μ is the dynamic viscosity, κ_a is the apparent permeability.

3.4. Permeability-porosity relation and analysis

The permeability-porosity plots for the porous materials by cold compaction and solid-state hot sintering are shown in Fig. 6. Both the experimental measurements (as the solid circles with error bars) and the simulation results (the solid squares for cold compaction and the solid triangles for compaction & sintering) are plotted in the same figure. For the simulation results, as stochastic factors are introduced in the initial distribution and structure generation of powder, multiple simulations have been performed for statistics for each case. In this work, every point of numerical results in Fig. 6 is obtained by averaging of five simulations, so that the statistical errors are thereby quantified. For the experimental measurements, every point stands for the average value, whose error bar is calculated based on 4 samples. For each sample, we conduct at least 5 measurements under different pressure differences. The largest pressure difference is imposed on 6.0% sample, whose value is 6 MPa. The smallest flow rate is 0.1 $\mu\text{L/s}$, which is measured in 6.0% sample, using 3.8 MPa pressure difference. The minimum scale value of

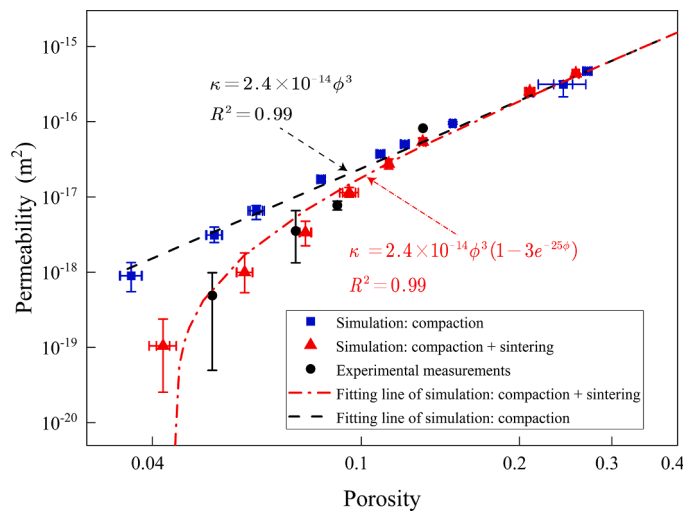


Fig. 6. The permeability-porosity plots by numerical simulations with and without sintering and by experimental measurements. The solid squares (blue) are the simulation results by compaction-only process. The solid triangles (red) are the simulation results by the compaction & sintering process. The solid circles (black) are the experimental data measured by the steady-state method. The dashed line (black) is the fitting line for the compaction-only data for a cubic scaling law with a coefficient of correlation, $R^2=0.99$. The simulation results by the compaction & sintering process agree well with the experimental results. The dash-dot line (red) is the fitting function of the simulation results for the compaction & sintering process, with a coefficient of correlation, $R^2=0.99$.

our soap-film flowmeter is 0.01 mL and for the smallest flow rate case, it takes 71 s for the total flow rate to reach the minimum scale value. Both the results from simulations and experiments indicate clearly that the permeability decreases significantly with the decrease of porosity, no matter with or without sintering, in this log-log plot of Fig. 6. For a high porosity, the permeability for compaction & sintering process merges with that for cold compaction-only process. When the porosity is lower than 0.1, the hot sintering process dramatically reduces the permeability of the porous materials, which has been illustrated by both numerical predictions and experimental data consistently.

For the porous materials by cold compaction only, the permeability appears linearly increasing with porosity in this log-log plot. The black dashed line stands for a fitting function, $\kappa = 2.4 \times 10^{-14} \phi^3$, with a correlation coefficient $R^2=0.99$, which means the permeability-porosity relation for compaction-only process follows a perfect cubic scaling law. This result also suggests that the powder materials with compaction-only process can be described by the famous Carman-Kozeny formula [23–25] well at a wide range of porosity.

Yet, when the hot solid-state sintering process is added after cold compaction, the permeability decreases dramatically, much faster than the cubic scaling law, as the porosity becomes lower than 0.1. The simulation results by the present numerical methods agree well with the experimental data, which means our numerical tool can capture the major behavior in the compaction & sintering processes. To summarize the compaction & sintering effects, we propose an empirical correlation function as:

$$\kappa = a\phi^3 f(\phi), \quad (9)$$

where $f(\phi)$ is the sintering correction factor which may depends majorly on powder properties and slightly on material plastic properties and so on. Here for simplicity it is supposed to be a function of only porosity, ϕ , and a is the fitted coefficient of the cubic scaling law for the cold compaction process. The function $f(\phi)$ needs to have two following features: (1) gradually approaching to unity as the porosity is high ($\phi>0.15$) to recover the cubic scaling law, and (2) sharply decaying to

zero when porosity is low ($\phi<0.05$). Following these two features, we propose an exponential form with fitting parameters on simulation and experimental data as:

$$\kappa = 2.4 \times 10^{-14} \phi^3 (1 - 3e^{-25\phi}), \quad (10)$$

with a coefficient of correlation, $R^2=0.99$. Instead of stepwise linear fitting in this log-log plot (i.e. stepwise scaling laws), this function continuously captures the permeability-porosity relation in the entire range of porosity, with asymptotically approaching to the cubic scaling law at high porosity.

The mechanism can be clearly illustrated by the pore size distribution in Fig. 7. The pore size is obtained by maximal ball algorithm, using open-source software ImageJ. For the cold compaction process without hot sintering, the percent of large pores decreases constantly with the reduction of porosity, from 0.32 to 0.11 and then 0.04. The proportion of small pores reaches the highest when the porosity reduces to 0.04, as shown in Fig. 7(a). The small pores connect the flow pathways, which helps to hold the cubic scaling law. Things change for the process with hot sintering, as shown in Fig. 7(b), that some small pores may vanish by sintering so that many of the large pores get isolated. The permeability decreases dramatically as a result by sintering effect. The difference between microstructure evolution processes with and without sintering makes the different relations of permeability-porosity. The numerical predictions by our simulation with hot sintering agree well with the experimental data in the entire porosity region, which suggests that the proposed curvature driving sintering process can captures the major mechanism of solid-state sintering.

4. Conclusions

In this work, a pore-scale numerical framework, including a DEM for powder cold compaction, a Cellular Automata algorithm with curvature-driving redistribution during hot sintering and an LBM for fluid flow simulation, is established to study the permeability of porous materials by the cold compaction and solid-state hot sintering processes. The numerical tools have been verified by analytical solutions for standard cases and validated by our experimental data for the permeability-porosity relation.

The results show that the cubic scaling law always holds for the porous materials by cold compaction, while the hot sintering process may dramatically decrease the permeability when the porosity is low. An exponential decay function has been proposed as a correction factor to the permeability-porosity relationship of materials by compaction & sintering processes, which predicts the permeability asymptotically approaching to the cubic scaling law at high porosity while agreeing well with both numerical and experimental data at low porosity.

Analysis of microstructure evolution shows that the small pores that connect large pores vanish by sintering so that the permeability decreases remarkably at low porosity. The excellent agreements between the present numerical predictions and the experimental measurements suggest that our numerical framework can capture the major behavior of the structural evolution in the cold compaction and solid-state sintering processes of powder packing materials and provide a powerful tool for analysis and optimization for material designs.

CRedit authorship contribution statement

Zhiguo Tian: Investigation, Software, Validation, Investigation, Writing – original draft. **Duzhou Zhang:** Investigation, Project administration. **Gang Zhou:** Validation, Writing – review & editing. **Shaohua Zhang:** Software, Validation. **Moran Wang:** Conceptualization, Supervision, Writing – review & editing, Project administration.

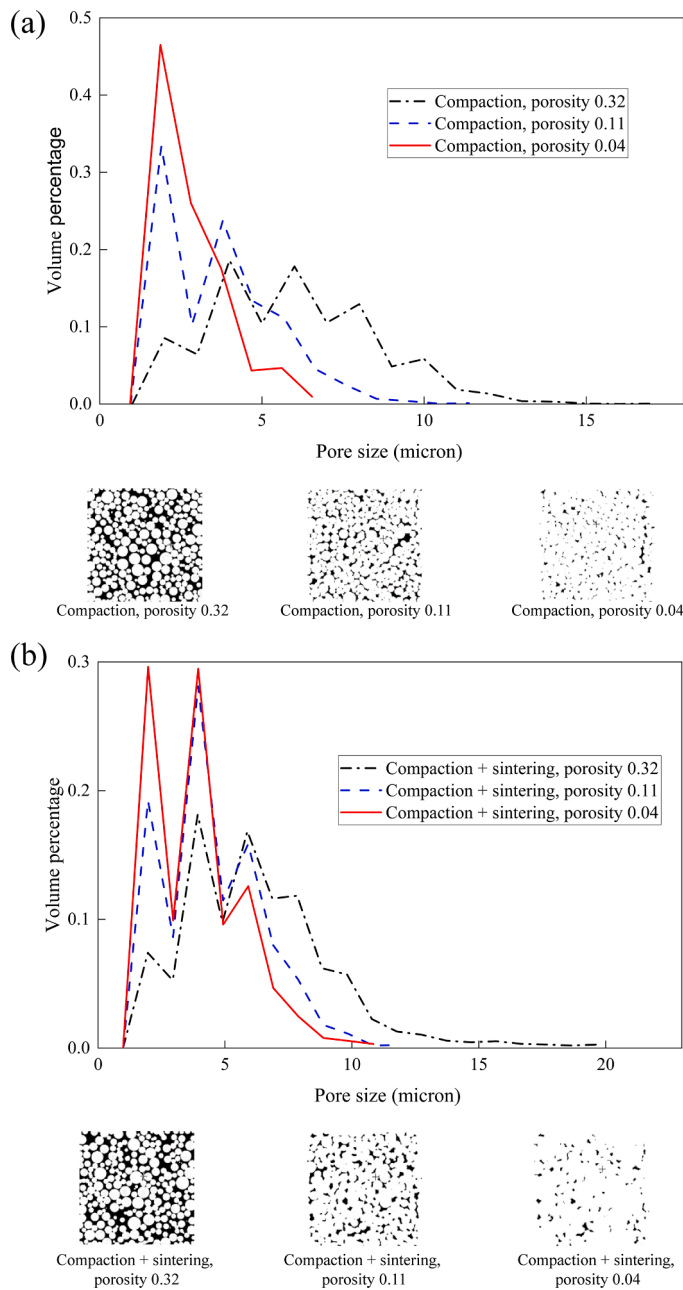


Fig. 7. The pore size distribution of the porous microstructures without and with sintering process. (a) is the pore size distribution of the microstructures by the compaction-only process with the porosity varying from 0.32, 0.11 to 0.04. The slices at the same position for the three cases are compared at the bottom. (b) is the pore size distribution of the microstructures by compaction & sintering process with the porosity varying from 0.32, 0.11 to 0.04. The slices at the same position for the three cases are compared at the bottom. The sintering process fills some small pores that connect large pores and make large pores isolated. The permeability is therefore dramatically decreased.

Declaration of Competing Interest

The authors declare that they have no known competing financial interests or personal relationships that could have appeared to influence the work reported in this paper.

The authors declare the following financial interests/personal relationships which may be considered as potential competing interests:

Data availability

No data was used for the research described in the article.

Acknowledgments

This work is financially supported by the NSF grant of China (No. U1837602, 11761131012) and the Tsinghua University Initiative Scientific Research Program.

References

- [1] Bernabe Y, Brace W, Evans B. Permeability, porosity and pore geometry of hot-pressed calcite. *Mech Mater* 1982;1(3):173–83.
- [2] Zhang S, Paterson MS, Cox SF. Porosity and permeability evolution during hot isostatic pressing of calcite aggregates. *J Geophys Res: Solid Earth* 1994;99(B8):15741–60.
- [3] Goyal S, Bhagwan J, Tomar SK. Elastic waves at the plane interface of swelling porous half-space and viscoelastic half-space with voids. *Int J Mech Sci* 2020;188:105942.
- [4] Wadsworth FB, Vasseur J, Llewellyn EW, Brown RJ, Tuffen H, Gardner JE, et al. A model for permeability evolution during volcanic welding. *J Volcanol Geotherm Res* 2021;409:107118.
- [5] Zhilyaev AP, Langdon TG. Using high-pressure torsion for metal processing: fundamentals and applications. *Prog Mater Sci* 2008;53(6):893–979.
- [6] Vrancken B, Thijs L, Kruth J-P, Van Humbeeck J. Heat treatment of Ti6Al4V produced by Selective Laser Melting: microstructure and mechanical properties. *J Alloy Compd* 2012;541:177–85.
- [7] Long X, Hu B, Feng Y, Chang C, Li M. Correlation of microstructure and constitutive behaviour of sintered silver particles via nanoindentation. *Int J Mech Sci* 2019:161.
- [8] Zhao M, Zhang DZ, Liu F, Li Z, Ma Z, Ren Z. Mechanical and energy absorption characteristics of additively manufactured functionally graded sheet lattice structures with minimal surfaces. *Int J Mech Sci* 2020:167.
- [9] Zhou M, Xu J, Zhou H. Evaluating the permeability properties of green bed in iron ore sintering using high resolution X-ray computed tomography and orthogonal array tests. *Powder Technol* 2020;375:360–8.
- [10] Zhou H, Lai Z, Lv L, Fang H, Meng H, Zhou M, et al. Improvement in the permeability of sintering beds by drying treatment after granulating sinter raw materials containing concentrates. *Adv Powder Technol* 2020;31(8):3297–306.
- [11] Ryan AG, Russell JK, Heap MJ, Zimmerman ME, Wadsworth FB. Timescales of porosity and permeability loss by solid-state sintering. *Earth Planet Sci Lett* 2020;549:116533.
- [12] Zhang C, Palko JW, Rong G, Pringle KS, Barako MT, Dusseault TJ, et al. Tailoring permeability of microporous copper structures through template sintering. *ACS Appl Mater Interfaces* 2018;10(36):30487–94.
- [13] Wadsworth FB, Vasseur J, Llewellyn EW, Dobson KJ, Colombier M, Von Aulock FW, et al. Topological inversions in coalescing granular media control fluid-flow regimes. *Phys Rev E* 2017;96(3):033113.
- [14] Wadsworth FB, Vasseur J, Scheu B, Kendrick JE, Lavallée Y, Dingwell DB. Universal scaling of fluid permeability during volcanic welding and sediment diagenesis. *Geology* 2016;44(3):219–22.
- [15] Sirono S-i. Planetsimal formation induced by sintering. *Astrophys J Lett* 2011;733(2):L41.
- [16] Zhang X-Y, Fang G, Leeflang S, Zadpoor AA, Zhou J. Topological design, permeability and mechanical behavior of additively manufactured functionally graded porous metallic biomaterials. *Acta Biomater* 2019;84:437–52.
- [17] Fiume E, Schiavi A, Orlygsson G, Bignardi C, Verné E, Bairo F. Comprehensive assessment of bioactive glass and glass-ceramic scaffold permeability: experimental measurements by pressure wave drop, modelling and computed tomography-based analysis. *Acta Biomater* 2021;119:405–18.
- [18] Erdim E, Akgiray Ö, Demir İ. A revisit of pressure drop-flow rate correlations for packed beds of spheres. *Powder Technol* 2015;283:488–504.
- [19] Walsh JB, Brace WF. The effect of pressure on porosity and the transport properties of rock. *J Geophys Res: Solid Earth* 1984;89(B11):9425–31.
- [20] Scheidegger AE. The physics of flow through porous media. The physics of flow through porous media. 3rd Edition. University of Toronto press; 2020.
- [21] Zhu W, Evans B, Bernabé Y. Densification and permeability reduction in hot-pressed calcite: a kinetic model. *J Geophys Res: Solid Earth* 1999;104(B11):25501–11.
- [22] Rahrah M, Lopez-Peña LA, Vermolen F, Meulenbroek B. Network-inspired versus Kozeny–Carman based permeability-porosity relations applied to Biot's poroelasticity model. *J Math Indu* 2020;10(1):1–21.
- [23] Carman PC. Fluid flow through granular beds. *Trans Inst Chem Eng* 1937;15:150–66.
- [24] Carman PC. Flow of gases through porous media. New York: Academic Press; 1956.
- [25] J K. Über kapillare leitung der wasser in boden. *J Royal Acad Sci, Vienna, Proc Class I* 1927;136:271–306.
- [26] Fink R, Krooss BM, Amann-Hildenbrand A. Stress-dependence of porosity and permeability of the Upper Jurassic Bossier shale: an experimental study. *Geol Soc, Lond, Spec Publicat* 2017;454(1):107–30.

- [27] Ryan AG, Russell JK, Heap MJ. Rapid solid-state sintering in volcanic systems. *Am Miner: J Earth Planet Mater* 2018;103(12):2028–31.
- [28] Fan Z, Hu C, Zhu Q, Jia Y, Zuo D, Duan Z. Three-dimensional pore characteristics and permeability properties of calcareous sand with different particle sizes. *Bull Eng Geol Environ* 2021;80(3):2659–70.
- [29] Okuma G, Tanaka S, Wakai F. Domain coarsening in viscous sintering as a result of topological pore evolution. *J Eur Ceram Soc* 2022;42(2):729–33.
- [30] Song S-B, Liu J-F, Yang D-S, Ni H-Y, Huang B-X, Zhang K, et al. Pore structure characterization and permeability prediction of coal samples based on SEM images. *J Nat Gas Sci Eng* 2019;67:160–71.
- [31] Sun S, Feng S, Ji C, Shi M, He X, Xu F, et al. Microstructural effects on permeability of Nitrocellulose membranes for biomedical applications. *J Memb Sci* 2020;595:117502.
- [32] Chmielewski M, Dutkiewicz J, Kaliński D, Lityńska-Dobrzyńska L, Pietrzak K, Strojny-Nędzka A. Microstructure and properties of hot-pressed molybdenum-alumina composites. *Arch Metall Mater* 2012;57:686–93.
- [33] Ashby MF. A first report on sintering diagrams. *Acta Metall* 1974;22(3):275–89.
- [34] Coble RL. Diffusion models for hot pressing with surface energy and pressure effects as driving forces. *J Appl Phys* 1970;41(12):4798–807.
- [35] German R. *Sintering: from empirical observations to scientific principles*. Butterworth-Heinemann; 2014.
- [36] Faouri SS, Mostaed A, Dean JS, Wang D, Sinclair DC, Zhang S, et al. High quality factor cold sintered Li₂MoO₄BaFe₁₂O₁₉ composites for microwave applications. *Acta Mater* 2019;166:202–7.
- [37] Salehi A, Pircheraghi G, Foudazi R. Pore structure evolution during sintering of HDPE particles. *Polymer (Guildf)* 2019;183:121865.
- [38] Liu T, Jin X, Wang M. Critical resolution and sample size of digital rock analysis for unconventional reservoirs. *Energies* 2018;11(7):1798.
- [39] Martin C, Schneider L, Olmos L, Bouvard D. Discrete element modeling of metallic powder sintering. *Scr Mater* 2006;55(5):425–8.
- [40] Cundall PA, Strack OD. A discrete numerical model for granular assemblies. *Geotechnique* 1979;29(1):47–65.
- [41] Nosewicz S, Rojek J, Pietrzak K, Chmielewski M. Viscoelastic discrete element model of powder sintering. *Powder Technol* 2013;246:157–68.
- [42] Shinagawa K. Simulation of grain growth and sintering process by combined phase-field/discrete-element method. *Acta Mater* 2014;66:360–9.
- [43] Paredes-Goyes B, Venkatesh AM, Jauffres D, Martin CL. Two-step sintering of alumina nano-powders: a discrete element study. *J Eur Ceram Soc* 2023;43(2):501–9.
- [44] Cundall PA. A computer model for simulating progressive, large-scale movement in blocky rock system. In: *Proceedings of the Proceedings of the International Symposium on Rock Mechanics*; 1971.
- [45] Guan K, Qin W, Liu Y, Yin X, Peng C, Lv M, et al. Evolution of porosity, pore size and permeate flux of ceramic membranes during sintering process. *J Memb Sci* 2016;520:166–75.
- [46] Martin CL, Yan Z, Jauffres D, Bouvard D, Bordia RK. Sintered ceramics with controlled microstructures: numerical investigations with the Discrete Element Method. *J Ceram Soc Jpn* 2016;124(4):340–5.
- [47] Hötzer J, Seiz M, Kellner M, Rheinheimer W, Nestler B. Phase-field simulation of solid state sintering. *Acta Mater* 2019;164:184–95.
- [48] Zhang D, Tian Z, Chen Z, Wu D, Zhou G, Zhang S, et al. Compaction effects on permeability of spherical packing. *Eng Comput (Swansea)* 2020;37(9):3079–96.
- [49] Du H-b, Dai F, Xu Y, Yan Z, Wei M-d. Mechanical responses and failure mechanism of hydrostatically pressurized rocks under combined compression-shear impacting. *Int J Mech Sci* 2020;165.
- [50] Wang Z, Ma D, Suo T, Li Y, Manes A. Investigation into different numerical methods in predicting the response of aluminosilicate glass under quasi-static and impact loading conditions. *Int J Mech Sci* 2021;196.
- [51] Kumar R, Rommel S, Jauffres D, Lhuissier P, Martin CL. Effect of packing characteristics on the discrete element simulation of elasticity and buckling. *Int J Mech Sci* 2016;110:14–21.
- [52] Harthong B, Jerier J-F, Richefeu V, Chareyre B, Doremus P, Imbault D, et al. Contact impingement in packings of elastic-plastic spheres, application to powder compaction. *Int J Mech Sci* 2012;61(1):32–43.
- [53] Mindlin RD. Compliance of elastic bodies in contact. *J Appl Mech* 1949;16(3):259–68.
- [54] Mindlin RD, Deresiewicz H. Elastic spheres in contact under varying oblique forces. *J Appl Mech* 1953;20(3):327–44.
- [55] Skrinjar L, Slavič J, Boltežar M. A review of continuous contact-force models in multibody dynamics. *Int J Mech Sci* 2018;145:171–87.
- [56] Zhu HP, Zhou ZY, Yang RY, Yu AB. Discrete particle simulation of particulate systems: theoretical developments. *Chem Eng Sci* 2007;62(13):3378–96.
- [57] Galindo-Torres S, Pedrosa D. Molecular dynamics simulations of complex-shaped particles using Voronoi-based spheropolyhedra. *Phys Rev E* 2010;81(6):061303.
- [58] Galindo-Torres SA, Pedrosa DM, Williams DJ, Li L. Breaking processes in three-dimensional bonded granular materials with general shapes. *Comput Phys Commun* 2012;183(2):266–77.
- [59] Pimienta PJ, Garboczi EJ, Carter WC. Cellular automaton algorithm for surface mass transport due to curvature gradients simulations of sintering. *Comput Mater Sci* 1992;1(1):63–77.
- [60] Qian YH, Dhumieres D, Lallemand P. Lattice BGK models for Navier-Stokes equation. *Europhys Lett* 1992;17(6BIS):479–84.
- [61] Wang J, Wang M, Li Z. A lattice Boltzmann algorithm for fluid-solid conjugate heat transfer. *Int J Therm Sci* 2007;46(3):228–34.
- [62] Chen S, Doolen GD. Lattice Boltzmann method for fluid flows. *Annu Rev Fluid Mech* 1998;30(1):329–64.
- [63] Ladd AJC, Verberg R. Lattice-Boltzmann simulations of particle-fluid suspensions. *J Stat Phys* 2001;104(5–6):1191–251.
- [64] Aidun CK, Clausen JR. Lattice-Boltzmann method for complex flows. *Annu Rev Fluid Mech* 2010;42:439–72.
- [65] Wang M, Chen S. Electroosmosis in homogeneously charged micro-and nanoscale random porous media. *J Colloid Interface Sci* 2007;314(1):264–73.
- [66] Wang M, Pan N. Predictions of effective physical properties of complex multiphase materials. *Mater Sci Eng: R: Rep* 2008;63(1):1–30.
- [67] Wang Z, Guo Y, Wang M. Permeability of high-Kn real gas flow in shale and production prediction by pore-scale modeling. *J Nat Gas Sci Eng* 2016;28:328–37.
- [68] Wang Z, Wang M, Chen S. Coupling of high Knudsen number and non-ideal gas effects in microporous media. *J Fluid Mech* 2018;840:56–73.
- [69] Ghasemi K, Siavashi M. Three-dimensional analysis of magnetohydrodynamic transverse mixed convection of nanofluid inside a lid-driven enclosure using MRT-LBM. *Int J Mech Sci* 2020;165.
- [70] Sobhani M, Tighchi HA, Esfahani JA. Attenuation of radiative heat transfer in natural convection from a heated plate by scattering properties of Al₂O₃ nanofluid: LBM simulation. *Int J Mech Sci* 2019;156:250–60.
- [71] Alizadeh A, Hsu W-L, Daiguji H, Wang M. Temperature-regulated surface charge manipulates ionic current rectification in tapered nanofluidic channel. *Int J Mech Sci* 2021;210.
- [72] Alizadeh A, Wang M. A generalized local grid refinement approach for modeling of multi-physicochemical transports by Lattice Boltzmann method. *Adv Appl Math Mech* 2019;11(2):312–37.
- [73] Kandhai D, Koponen A, Hoekstra AG, Kataja M, Timonen J, Sloom PMA. Lattice-Boltzmann hydrodynamics on parallel systems. *Comput Phys Commun* 1998;111(1–3):14–26.
- [74] Pan CX, Prins JF, Miller CT. A high-performance lattice Boltzmann implementation to model flow in porous media. *Comput Phys Commun* 2004;158(2):89–105.
- [75] Šmilauer V, Catalano E, Chareyre B, Dorofeenko S, Duriez J, Gladky A, et al. *Yade* documentation. 3rd ed. 2021.
- [76] Wang Z, Jin X, Wang X, Sun L, Wang M. Pore-scale geometry effects on gas permeability in shale. *J Nat Gas Sci Eng* 2016;34:948–57.
- [77] Liu GZ, Liu FL, Li M, Jin X, Lv WF, Liu Q, et al. Lattice boltzmann model for upscaling of flow in heterogeneous porous media based on darcy's law. *J Porous Media* 2019;22(9):1131–9.
- [78] Klinkenberg L. The permeability of porous media to liquids and gases. *Am Petrol Inst, Drill Product Pract* 1941;2:200–13.